Quantum Spin Hall Effect and Topological Field Effect Transistor in Two-Dimensional Transition Metal Dichalcogenides

Citation: Qian, X., J. Liu, L. Fu, and J. Li. "Quantum Spin Hall Effect in Two-Dimensional Transition Metal Dichalcogenides." Science (November 2014): n. pag.

As Published: http://dx.doi.org/10.1126/science.1256815

Publisher: American Association for the Advancement of Science (AAAS)

Persistent URL: http://hdl.handle.net/1721.1/91679

Version: Author's final manuscript: final author's manuscript post peer review, without publisher's formatting or copy editing

Quantum Spin Hall Effect and Topological Field Effect Transistor in Two-Dimensional Transition Metal Dichalcogenides

Xiaofeng Qian[1,†], Junwei Liu[2,†], Liang Fu[2,*], and Ju Li[1,*]

[1]Department of Nuclear Science and Engineering and Department of Materials Science and Engineering, Massachusetts Institute of Technology, Cambridge, Massachusetts 02139, USA.

[2]Department of Physics, Massachusetts Institute of Technology, Cambridge, Massachusetts 02139, USA.

*Correspondence to: liangfu@mit.edu and liju@mit.edu.

†These authors contributed equally to this work.

We predict a new class of large-gap quantum spin Hall insulators in two-dimensional transition metal dichalcogenides with 1T' structure, namely, 1T'-MX_2 with M=(Mo, W) and X=(S, Se, and Te) by first-principles calculations. The structural distortion causes an intrinsic band inversion between chalcogenide-*p* and metal-*d* bands, and spin-orbit coupling opens a gap at finite momentum, which is highly tunable by vertical electric field. This motivates us to propose a topological field effect transistor made of these atomic-layer van der Waals heterostructures with multiple topologically protected transport channels, which can be rapidly switched off by electric field through topological phase transition instead of carrier depletion.

One Sentence Summary: Electric-field tunable quantum spin Hall insulators in 1T' 2D transition metal dichalcogenides enables the construct of vdW topological field effect transistor.

The discovery of graphene (*1*) leads to vigorous explorations of two-dimensional (2D) materials (*2*), revealing a wide range of extraordinary properties (*3-5*) and functionalities (*6, 7*). Owing to atomic thickness, 2D materials can be horizontally patterned through chemical and mechanical techniques (*8*). Moreover, the weak van der Waals (vdW) interaction between adjacent layers enables vertical stacking of different 2D materials, forming vdW heterostructures (*9*), offering unprecedented opportunities for exploring quantum electronics at nanoscale.

Quantum Spin Hall (QSH) insulators (*10-18*) have an insulating bulk but conducting edge states that are topologically protected from backscattering by time reversal symmetry. Quantized conductance through QSH edge states have been experimentally demonstrated in HgTe/CdTe (*15, 16*) and InAs/GaSb (*19, 20*) quantum wells. This could in principle provide an alternative route to quantum electronic devices with low dissipation. However, the realization of such QSH-based devices for practical applications is impeded by three critical factors: (a) band gaps of existing QSH insulators are too small, which limits the operating regime to low temperatures. This has motivated intensive efforts to search for large-gap QSH insulators (*21-26*); (b) the small number of conducting channels (e^2/h per edge) results in a small signal-to-noise ratio; and (c) efficient methods of fast ON/OFF switching are lacking.

Here by employing first-principles calculations, we show that 2D materials can provide a practical platform for developing novel topological electronic devices that may potentially overcome the above hurdles. Specifically, based on first-principles calculations, we find a new class of large-gap (~0.1eV) QSH insulators in 2D transition metal dichalcogenides (TMDCs) MX_2 with M=(Mo, W) and X = (S, Se, Te). We demonstrate the possibility of a novel vdW-heterostructured topological field effect transistor (vdW-TFET) made of 2D atomic layer materials. Our device exhibits a parametrically enhanced conductance through QSH edge channels in the ON state, and can be rapidly switched OFF via a topological phase transition by applying a vertical electric field. Our findings of electrically configurable QSH devices have potential applications in low-power quantum electronics and spintronics, and may enable topological quantum computing based on Majorana fermions (*27-30*).

Monolayer TMDCs (*31*), MX_2 with M = (Mo, W) and X = (S, Se, Te), possess a variety of polytypic structures such as 1H, 1T, and 1T' (*32, 33*) shown in Fig. 1. The most studied 1H structure is a sandwich of three planes of 2D hexagonally packed atoms, X-M-X, forming ABA stacking. In contrast, three atomic planes in the 1T structure form ABC stacking. It has been known that the 1T structure in MX_2 is typically unstable in free-standing condition and undergoes a spontaneous lattice distortion in the *x* direction to form a period-doubling 2×1 distorted structure, i.e., the 1T' structure, consisting of one-dimensional zigzag chains along the *y* direction shown in Fig. 1C (*33*), which is the subject of this work.

The electronic structures of 1T'-MX_2 were obtained by many-body perturbation theory calculations (see Methods in Supplementary Materials). Figure 2A shows a typical band structure of 1T'-MX_2 using 1T'-MoS_2 as an example, and the results of the other five compounds are shown in Supplementary Fig. S1. Unlike its 1H or 1T counterparts, 1T'-MoS_2 is a

semiconductor with a fundamental gap (E_g) of about 0.08 eV, located at $\Lambda = \pm(0, 0.146)$ Å^{-1} (red dots in Fig. 2B). The conduction and valence bands display a camelback shape near Γ in the 2D Brillouin zone (BZ, see Fig. 2B), suggestive of band inversion with a large inverted gap (2δ) at Γ over 0.6 eV. The fundamental gap (E_g) and inverted gap (2δ) of all six 1T'-MX_2 are shown in Fig. 2C, and listed in Supplementary Table S1. Since the 1T' structure has inversion symmetry, we calculated the Z_2 index based on the parity criterion (*34*) of valence bands (Supplementary Fig. S2) and found Z_2=1, establishing the QSH insulator phase in 2D 1T'-MX_2.

To understand the origin of the inverted band structure near Γ, we analyzed their orbital characters, and found the valence band mainly consists of metal *d*-orbitals and the conduction band mainly consists of chalcogenide *p*-orbitals, as expected. But the unexpected band inversion arises from the period doubling of metal chain in the 1T' structure, which lowers the metal *d* orbital below chalcogenide *p* orbital (Fig. 2A) around Γ. The large band inversion at Γ (0.6eV) exists with/without spin-orbit interaction and with/without external electric field, and is an *intrinsic* character of the 1T' structure. Without including spin-orbit coupling, this band inversion leads to the appearance of two Dirac cones centered at finite momentum on Y-Γ-Y in 2D. Spin-orbit coupling then opens up a fundamental gap of 0.08eV at the Dirac points (see the inset of Fig. 2A and Supplementary Materials Fig. S3), leading to QSH insulator in a similar mechanism as Kane-Mele model for graphene (*12*), as we show by a low-energy $\boldsymbol{k} \cdot \boldsymbol{p}$ Hamiltonian in Supplementary Methods and Fig. S4. In addition to MoS_2, we found that all other five 1T'-MX_2 have Z_2 nontrivial band topology.

The QSH insulator phase in 2D 1T'-MX_2 leads to helical edge states that are protected from localization and elastic backscattering by TRS. Figure 2D displays the edge states of 1T'-MoS_2 obtained from surface Green's function calculations (see Supplementary Materials), showing a pair of counter-propagating edge modes with a high velocity of $\sim 1.0\times10^5$m/s crossing at Γ, which carries opposite spin polarizations. From the local density of states in Fig. 2E, we find the decay length of these helical edge states is as short as 5 nm, allowing a 2D domain's Z_2 topology to be preserved down to nanoelectronic feature sizes before edge interference takes over. In addition, the short localization length can significantly reduce scattering with bulk states (*35*), hence increasing the transport lifetime. Similar results are found for five other TMDCs, as shown in the Supplementary Figs. S5 and S6.

Remarkably, the inverted bands (chalcogenide *p* – metal *d*) located on well-separated planes offers us a facile mechanism to control topological electronic properties by electric field, which is highly desirable for vdW devices. Based on first-principles calculations, we found vertical electric field indeed induces topological phase transition in 1T'-MX_2, as shown in Fig. 3 for 1T'-MoS_2. Here the electric field breaks inversion symmetry and introduces strong Rashba splitting of the doubly degenerate bands near the fundamental gap E_g at the Λ points. As the field increases, E_g first decreases to zero at a critical field strength of 0.142 V/Å, and then reopens (see Fig. 4A). This gap-closing transition induces a topology change to a trivial phase (*13, 36*), leading to the destruction of helical edge states.

The above findings enable an all-electrical control of the ON/OFF charge/spin conductance of helical edge states, which have significant implications on QSH-based devices (*37-42*). Here we propose a topological field effect transistor (TFET) based on vdW heterostructures of 2D TMDCs and 2D wide-gap insulators. The schematic device is shown in Fig. 4B, where the top and bottom gates supply the vertical electric field to control the ON/OFF function. 2D wide-gap insulators such as hexagonal boron nitride (*h*BN) (*43*) electrically insulate adjacent QSH layers, hence protect parallel helical edge channels from being gapped by inter-layer hybridization. This can parametrically increase the number of edge transport channels. Under ideal conditions, this device will support dissipationless charge/spin transport in the ON state (Z_2=1) with a quantized conductance of $2Ne^2/h$, where N is the number of QSH layers. Applying a moderate electric field will transform 1T'-MX_2 into an ordinary insulator (Z_2=0) and turn the edge conduction OFF, see Fig. 4A.

The proposed vdW-TFET may possess important technical advantages, due to its novel operation mechanism that is fundamentally different from traditional metal-oxide-semiconductor field-effect transistors (MOS-FET). MOS-FET works by injecting/depleting free carrier beneath the gate, with a *RC*-type response time influenced by carrier concentration and mobility in the working channel, while our vdW-TFET works by switching the presence/absence of topologically protected conduction channels without changing the carrier density. The electric field induced topological phase transition can happen very rapidly, with electronic response timescale (*44, 45*). In addition, the vdW heterostructure and the 2D nature of vdW-TFET make it convenient to both *vertically* and *horizontally* pattern devices at large scale. The short decay length of helical edge states allows the minimum feature size of vdW-TFET to be ~10 nm, enabling high device density on a chip. TFET devices of such nanoscale size have large surface-to-bulk ratio, which will greatly reduce the contribution of thermally populated bulk carriers to the total electric current and hence enhance the ON/OFF ratio. The predicted QSH insulators and their vdW-heterostructures provide another choice for the realization of other novel low-dissipation quantum electronics and spintronics (*37-42*).

From materials perspective, the 1T' structure in monolayer MoS_2 has recently been observed in high-resolution TEM experiments (*33*). We have checked the structural stability of 1T' by carrying out first-principles calculations (see Supplementary Fig. S7). While MoS_2, $MoSe_2$, $MoTe_2$, WS_2 and WSe_2 are more stable in the commonly found 1H structure, we find there exists a large energy barrier of more than 1eV/MX_2 between 1T' and 1H for all MX_2, suggesting that the 1T' structure can be stabilized under appropriate chemical (*46*), thermal, or mechanical conditions. Moreover, we found the 1T structure is unstable and will spontaneously relax to 1T' like in Peierls distortion. We also verified the stability of the 1T' structure by computing its phonon dispersion (Supplementary Fig. S8). The absence of imaginary frequency throughout the 2D BZ provides a direct evidence of the structural stability in all 1T'-MX_2.

Encouragingly, the desired 1T' structure with intrinsic band inversion is the natural ground-state structure of WTe_2 (*31*), also confirmed by our stability calculation. Although monolayer WTe_2 was found to be a semimetal from our calculation, the small negative fundamental gap can be easily lifted by a tensile strain as small as ~1% shown in Supplementary Fig. S9. We also found

that *h*BN used as a dielectric in the aforementioned vdW-TFET device has little effect on the electronic structure of 1T'-WTe_2 near the Fermi level (see Supplementary Fig. S10). These attractive features make WTe_2 potentially the most promising 2D TMDC for realizing the QSH effect and related vdW devices.

References and Notes:

1. K. S. Novoselov *et al.*, *Science* **306**, 666-669 (2004).
2. K. S. Novoselov *et al.*, *Proc. Natl. Acad. Sci. U. S. A.* **102**, 10451-10453 (2005).
3. C. Lee, X. Wei, J. W. Kysar, J. Hone, *Science* **321**, 385-388 (2008).
4. A. H. Castro Neto, F. Guinea, N. M. R. Peres, K. S. Novoselov, A. K. Geim, *Rev. Mod. Phys.* **81**, 109-162 (2009).
5. K. F. Mak, C. Lee, J. Hone, J. Shan, T. F. Heinz, *Phys. Rev. Lett.* **105**, 136805 (2010).
6. Q. H. Wang, K. Kalantar-Zadeh, A. Kis, J. N. Coleman, M. S. Strano, *Nature Nanotech.* **7**, 699-712 (2012).
7. J. Feng, X. Qian, C.-W. Huang, J. Li, *Nature Photon.* **6**, 866-872 (2012).
8. K. S. Kim *et al.*, *Nature* **457**, 706-710 (2009).
9. A. K. Geim, I. V. Grigorieva, *Nature* **499**, 419-425 (2013).
10. D. Kong, Y. Cui, *Nature Chemistry* **3**, 845-849 (2011).
11. K. Yang, W. Setyawan, S. Wang, M. Buongiorno Nardelli, S. Curtarolo, *Nature Mater.* **11**, 614-619 (2012).
12. C. L. Kane, E. J. Mele, *Phys. Rev. Lett.* **95**, 226801 (2005).
13. C. L. Kane, E. J. Mele, *Phys. Rev. Lett.* **95**, 146802 (2005).
14. B. A. Bernevig, S.-C. Zhang, *Phys. Rev. Lett.* **96**, 106802 (2006).
15. B. A. Bernevig, T. L. Hughes, S.-C. Zhang, *Science* **314**, 1757-1761 (2006).
16. M. König *et al.*, *Science* **318**, 766-770 (2007).
17. M. Z. Hasan, C. L. Kane, *Rev. Mod. Phys.* **82**, 3045-3067 (2010).
18. X.-L. Qi, S.-C. Zhang, *Rev. Mod. Phys.* **83**, 1057-1110 (2011).
19. L. Du, I. Knez, G. Sullivan, R.-R. Du, http://arxiv.org/abs/1306.1925, (2013).
20. C. Liu, T. L. Hughes, X.-L. Qi, K. Wang, S.-C. Zhang, *Phys. Rev. Lett.* **100**, 236601 (2008).
21. S. Murakami, *Phys. Rev. Lett.* **97**, 236805 (2006).
22. C.-C. Liu, W. Feng, Y. Yao, *Phys. Rev. Lett.* **107**, 076802 (2011).
23. D. Xiao, W. Zhu, Y. Ran, N. Nagaosa, S. Okamoto, *Nature Commun.* **2**, 596-596 (2011).
24. Y. Xu *et al.*, *Phys. Rev. Lett.* **111**, 136804 (2013).
25. H. Weng, X. Dai, Z. Fang, *Physical Review X* **4**, 011002 (2014).
26. M. A. Cazalilla, H. Ochoa, F. Guinea, *Phys. Rev. Lett.* **113**, 077201 (2014).
27. L. Fu, C. L. Kane, *Phys. Rev. Lett.* **100**, 096407 (2008).
28. L. Fu, C. L. Kane, *Phys. Rev. B* **79**, 161408 (2009).
29. S. Mi, D. I. Pikulin, M. Wimmer, C. W. J. Beenakker, *Phys. Rev. B* **87**, 241405 (2013).
30. J. Alicea, *Rep. Prog. Phys.* **75**, 076501 (2012).
31. J. A. Wilson, A. D. Yoffe, *Advances in Physics* **18**, 193-335 (1969).
32. J. Heising, M. G. Kanatzidis, *J. Am. Chem. Soc.* **121**, 11720-11732 (1999).
33. G. Eda *et al.*, *ACS Nano* **6**, 7311 (2012).

34. L. Fu, C. L. Kane, *Phys. Rev. B* **76**, 045302 (2007).
35. J. I. Väyrynen, M. Goldstein, L. I. Glazman, *Phys. Rev. Lett.* **110**, 216402 (2013).
36. S. Murakami, *New J. Phys.* **9**, 356 (2007).
37. J. Wunderlich *et al.*, *Science* **330**, 1801-1804 (2010).
38. D. Pesin, A. H. MacDonald, *Nature Mater.* **11**, 409-416 (2012).
39. F. Mahfouzi, N. Nagaosa, B. K. Nikolić, *Phys. Rev. Lett.* **109**, 166602 (2012).
40. C. Brüne *et al.*, *Nature Phys.* **8**, 485-490 (2012).
41. C. H. Li *et al.*, *Nature Nanotech.* **9**, 218-224 (2014).
42. A. R. Mellnik *et al.*, *Nature* **511**, 449-451 (2014).
43. C. R. Dean *et al.*, *Nature Nanotech.* **5**, 722-726 (2010).
44. J. Liu *et al.*, *Nature Mater.* **13**, 178-183 (2014).
45. P. Michetti, B. Trauzettel, *Appl. Phys. Lett.* **102**, 063503 (2013).
46. M. Calandra, *Phys. Rev. B* **88**, 245428 (2013).

Acknowledgments: We acknowledge support from NSF under Award DMR-1120901 (X.Q. and J.L.), U.S. Department of Energy, Office of Basic Energy Sciences, Division of Materials Sciences and Engineering under Award DE-SC0010526 (L.F.), and the STC Center for Integrated Quantum Materials, NSF Grant No. DMR-1231319 (J.W.L). Computational time on the Extreme Science and Engineering Discovery Environment (XSEDE) under the grant number TG-DMR130038 and TG-DMR140003 is gratefully acknowledged. X.Q. and J.W.L. contributed equally to this work.

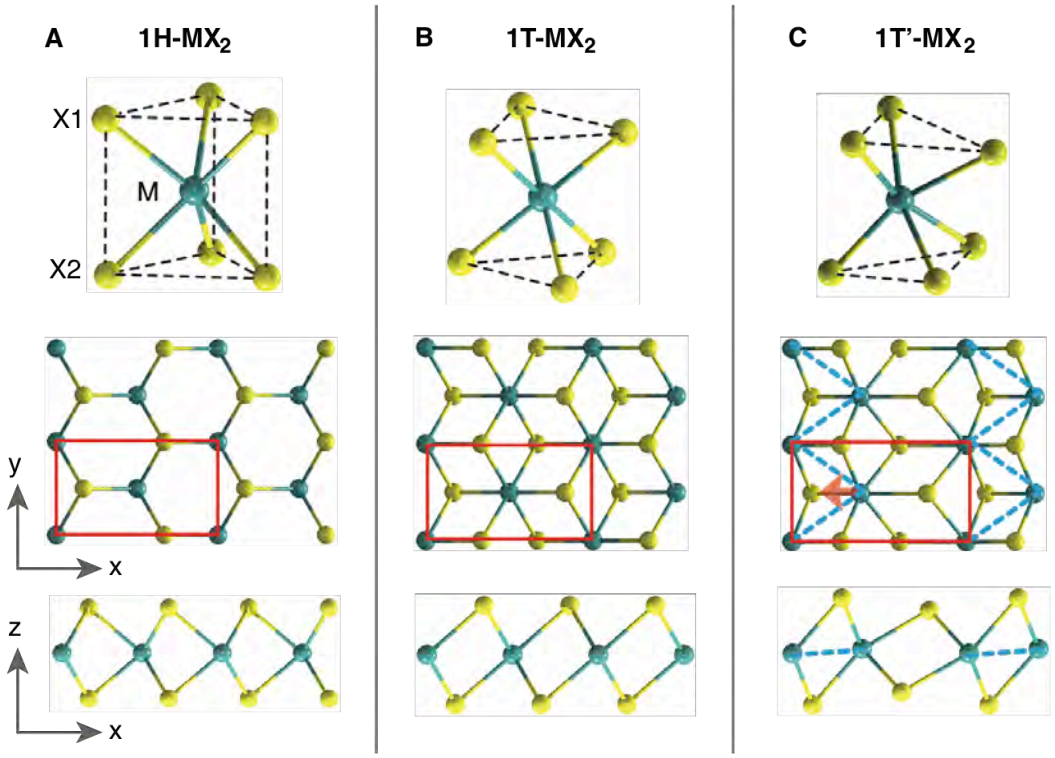

Fig. 1. Atomistic structure of monolayer transition metal dichalcogenide MX_2. M stands for (Mo,W) and X stands for (S, Se, Te). (**A**) 1H-MX_2 in ABA stacking with $P\bar{6}m2$ space-group. (**B**) 1T-MX_2 in ABC stacking with $P\bar{3}m2$ space group. (**C**) 1T'-MX_2, distorted 1T-MX_2, where the distorted M atoms form one-dimensional zigzag chains indicated by the dashed blue line. Unit cell is indicated by red rectangles.

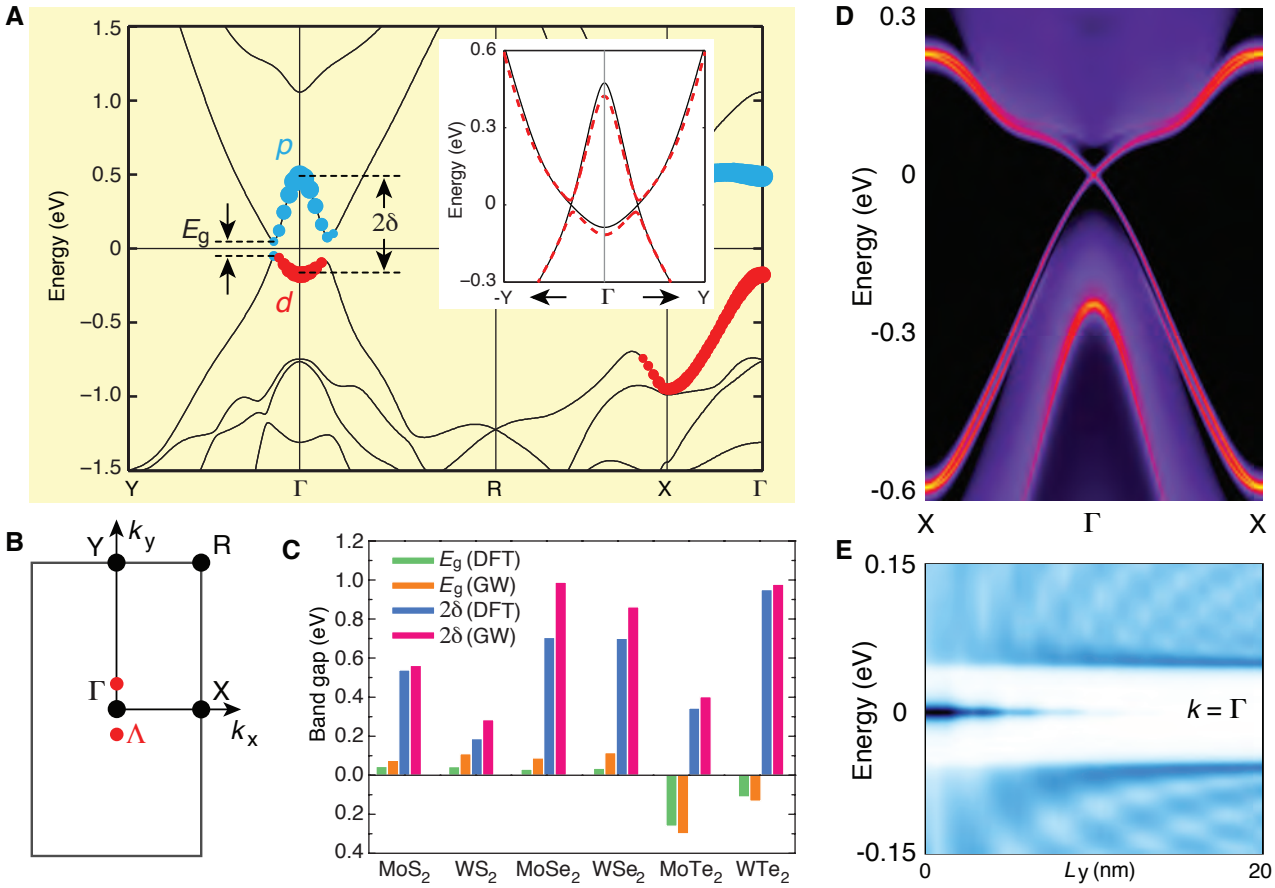

Fig. 2. Electronic structures of 1T'-MX_2. (**A**) Band structure and (**B**) Brillouin zone of 1T'-MoS_2. E_g: fundamental gap. 2δ: inverted gap. The inset compares band structures with (red dashed line) and without spin-orbit coupling (black solid line). Four time-reversal invariant momenta are marked by black dots and labeled as Γ, X, Y, and R. The locations of fundamental gap are marked by red dots and labeled by Λ. (**C**) Fundamental gap (E_g) and inverted gap (2δ) of all six 1T'-MX_2. Detailed values are listed in Supplementary Table S1. (**D**) Edge density of states and (**E**) local density of states at Γ point as a function of distance away from the edge (L_y) away from the edge. A sharp peak from edge states appears in the gap with a decay length of ~5 nm.

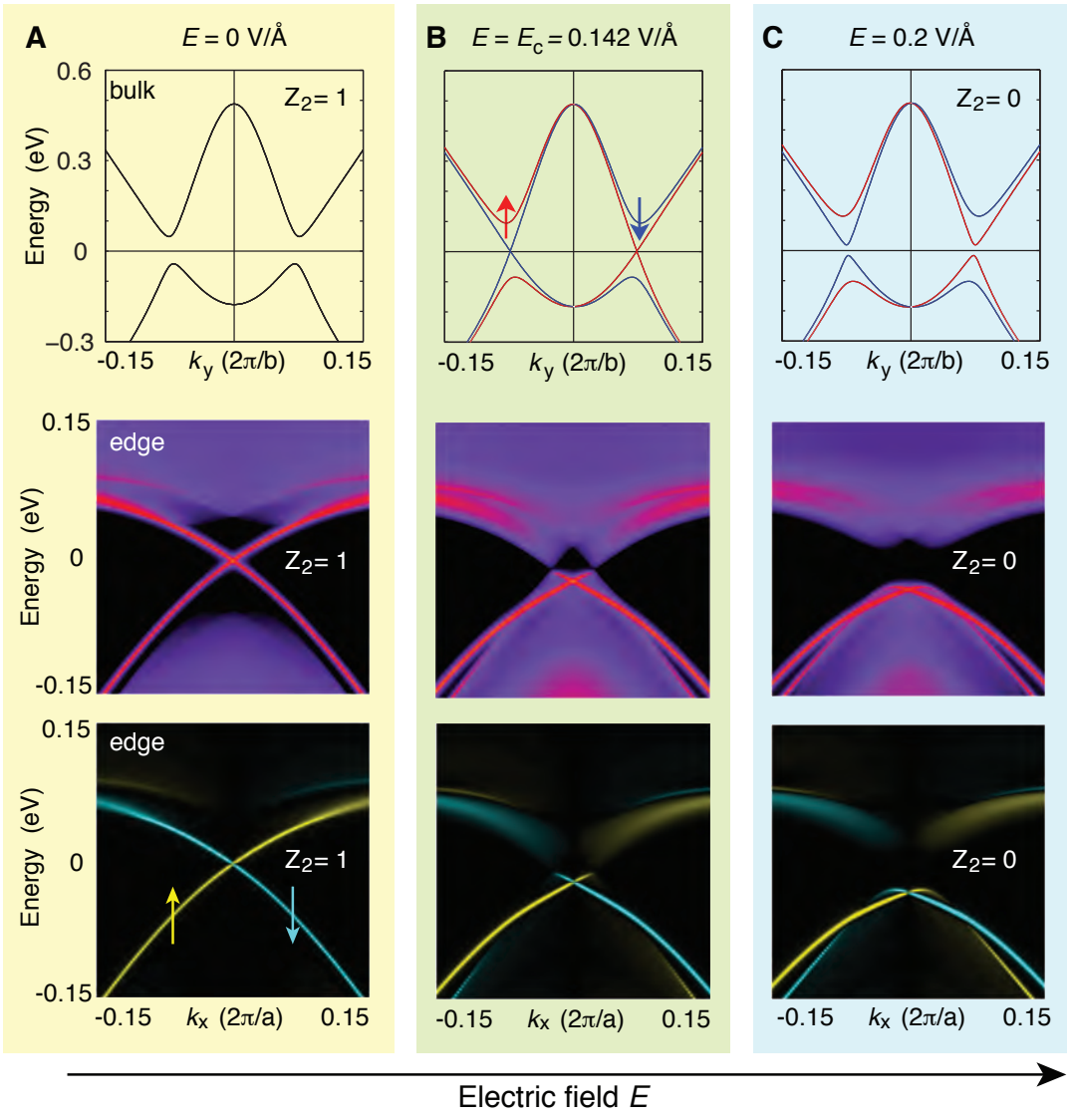

Fig. 3. Vertical electric field induced topological phase transition in monolayer 1T'-MoS_2 under electric field of (A) 0, (B) 0.142, and (C) 0.2 V/Å, respectively. The first, second, and third row show the bulk band structure, edge density of states, and edge spin polarization, respectively.

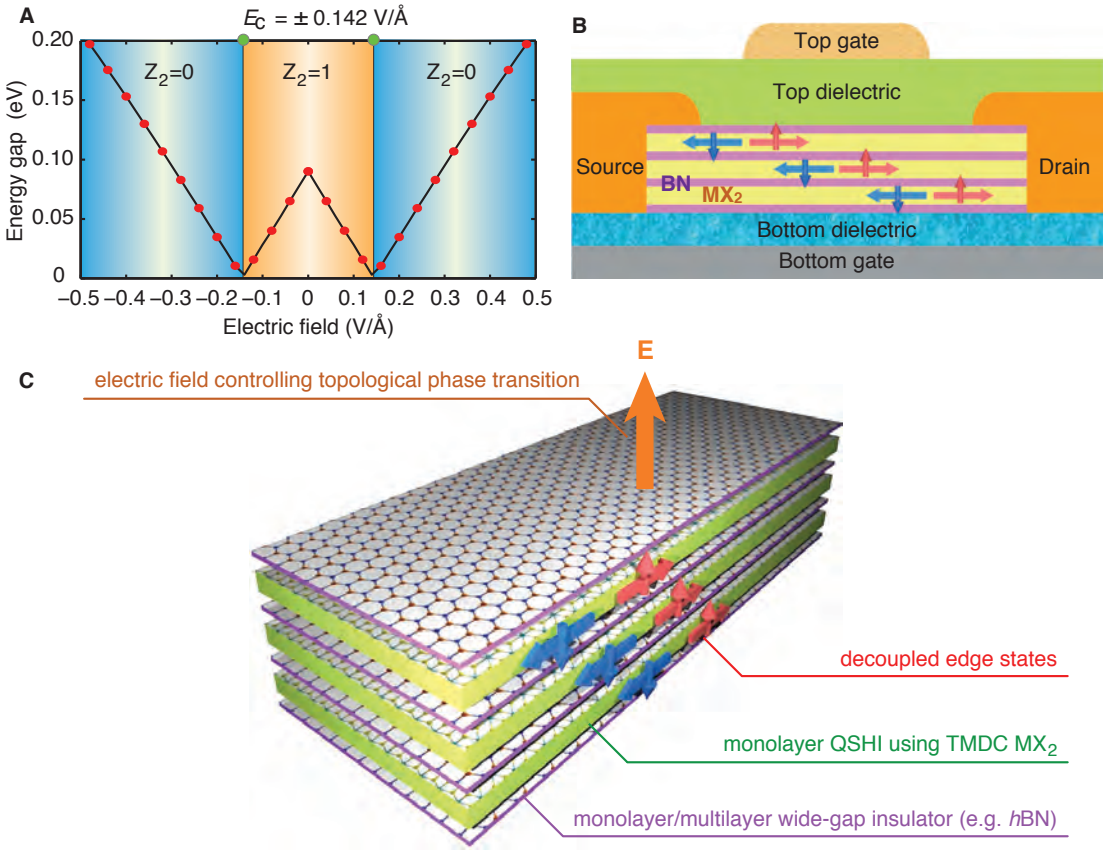

Fig. 4. VdW-heterostructured topological field effect transistor (vdW-TFET). (**A**) Topological phase diagram of 1T'-MoS_2 as function of vertical electric field. The critical field strength is ±0.142 eV/Å, marked by two green dots. (**B**) Schematic of vdW-TFET. The central component (**C**) is the vdW heterostructure of alternating monolayer 1T'-MX_2 and mono-/multi-layer wide-gap insulators such as *h*BN. Carriers (charge or spin) are injected from source electrode and ejected from drain electrode. ON/OFF switch is controlled by vertical electric field through the top and bottom gates. Mono-/multi-layer wide-gap insulators effectively screen the interaction between adjacent MX_2 layers, preventing them from detrimental topological phase change and parametrically increasing the number of edge channels and the signal-to-noise ratio.

Supplementary Materials:

Supplementary Methods

Table S1

Figures S1-S10

References

Supplementary Materials for

Quantum Spin Hall Effect and Topological Field Effect Transistor in Two-Dimensional Transition Metal Dichalcogenides

Xiaofeng Qian[1,†], Junwei Liu[2,†], Liang Fu[2,*], and Ju Li[1,*]

[1]Department of Nuclear Science and Engineering and Department of Materials Science and Engineering, Massachusetts Institute of Technology, Cambridge, Massachusetts 02139, USA.

[2]Department of Physics, Massachusetts Institute of Technology, Cambridge, Massachusetts 02139, USA.

*Correspondence to: liangfu@mit.edu and liju@mit.edu.

†These authors contributed equally to this work.

This PDF file includes:

Methods:

1. Ground-state atomic structures of monolayer transition metal dichalcogenides 1T'-MX_2

Ground-state atomic structures of all six monolayer transition metal dichalcogenides 1T'-MX_2 were fully relaxed using first-principles density functional theory (DFT) (*1, 2*). The calculations were performed by the Vienna Ab initio Simulation Package (*3, 4*) with projector-augmented wave method (*5*) and exchange-correlation functional in the Perdew-Berke-Ernzerhof's form (*6*) within the generalized-gradient approximation (*7, 8*). We used an energy cutoff of 400 eV and maximum residual force less than 0.001 eV/Å. The Monkhorst-Pack $\boldsymbol{k}$-point sampling (*9*) of $8\times8\times1$ was adopted for the Brillouin zone integration, and a large vacuum region of more than 16 Å was applied to the plane normal direction in order to minimize image interactions from the periodic boundary condition. Moreover, phonon dispersion curves were calculated by first-principles density-functional perturbation theory and the results are shown in Fig. S8 for all six materials.

2. Bulk electronic structure of monolayer transition metal dichalcogenides 1T'-MX_2

We first computed the electronic band structures of monolayer transition metal dichalcogenides 1T'-MX_2 using first-principles DFT. Since the calculated DFT band structures only provide qualitative electronic structure for quasi-particles such as electrons and holes, we further computed quasi-particle band structures using more accurate method, namely, many-body perturbation theory within Hedin's G_0W_0 approximation (*10, 11*). The results are shown in Fig. 2A for monolayer 1T'-MoS_2 and Fig. S1 for all six materials. Fundamental gap (E_g) and inverted gap (2δ) of monolayer transition metal dichalcogenides 1T'-MX_2 are collected in Table S1 and Fig. 2C.

3. Electronic structure of edge states in monolayer transition metal dichalcogenides 1T'-MX_2

The Z_2 trivial/nontrivial band topology has distinct consequence on the helical edge state. To reveal the helical edge states of monolayer 1T'-MX_2 explicitly, we performed iterative Green's function calculations (*12*) using tight-binding Hamiltonian (*13, 14*) constructed from many-body perturbation theory with the GW approximation (*10, 11*), where we extracted the edge density of states, spin polarization, and decay length of the helical edge states. The results are shown in Fig. 3 for monolayer 1T'-MoS_2 and Fig. S5 and Fig. S6 for all six materials. Furthermore, to investigate the effect of vertical electric field on the electronic structure of monolayer 1T'-MoS_2 QSHI, we introduce a corresponding change in the diagonal elements of first-principles tight-binding Hamiltonian. This approach is validated by comparing it with direct self-consistent first-principles calculations under the same electric field. In addition, we found the electric field has negligible impact on ionic positions.

4. Z_2 invariant of monolayer transition metal dichalcogenides 1T'-MX_2

The Z_2 invariant was obtained by explicitly calculating band parity of the materials with inversion symmetry (*15*). The results are shown in Fig. S2 for all six materials with inversion center located at the middle of the bond formed by two transition metal atoms in the quasi-one

dimensional chain along y direction. We also cross-checked all the results by the *n*-field method (*16*).

5. $\boldsymbol{k \cdot p}$ model for monolayer transition metal dichalcogenides 1T'-MX_2

The valence band mainly consists of *d*-orbitals of M atoms, while the conduction band mainly consists of p_y-orbitals of X atoms. The origin of such inversion roots in the formation of quasi-one dimensional transition metal chains in the 1T' structure, which lowers M's *d* orbital below p X's *p* to with respect to the original 1T structure, leading to the band inversion at Γ point (Fig. S3). By analyzing the symmetry properties of these bands, we develop a low-energy $\boldsymbol{k \cdot p}$ Hamiltonian for 1T'-MX_2,

$$H = \begin{pmatrix} E_p(k_x, k_y) & 0 & -iv_1\hbar k_x & v_2\hbar k_y \\ 0 & E_p(k_x, k_y) & v_2\hbar k_y & -iv_1\hbar k_x \\ iv_1\hbar k_x & v_2\hbar k_y & E_d(k_x, k_y) & 0 \\ v_2\hbar k_y & iv_1\hbar k_x & 0 & E_d(k_x, k_y) \end{pmatrix},$$

where $E_p = -\delta - \frac{\hbar^2 k_x^2}{2m_x^p} - \frac{\hbar^2 k_y^2}{2m_y^p}$, and $E_d = \delta + \frac{\hbar^2 k_x^2}{2m_x^d} + \frac{\hbar^2 k_y^2}{2m_y^d}$. Here $\delta < 0$ corresponds to the *d*-*p* band inversion. By fitting with first-principles band structure in Fig. 2A, we obtain the parameters: $\delta = -0.33$ eV, $v_1 = 3.87\times10^5$ m/s, $v_2 = 0.46\times10^5$ m/s, $m_x^p = 0.50\, m_e$, $m_y^p = 0.16\, m_e$, $m_x^d = 2.48\, m_e$, and $m_y^d = 0.37\, m_e$, where m_e is the free electron mass. Fig. S4 shows the comparison of band structures obtained from first-principles GW calculations and the $\boldsymbol{k \cdot p}$ model.

1T' phase	Fundamental gap (E_g, eV)		Inverted gap (2δ, eV)	
	DFT-PBE	G_0W_0	DFT-PBE	G_0W_0
MoS_2	0.045	0.076	0.540	0.562
WS_2	0.044	0.110	0.187	0.284
$MoSe_2$	0.031	0.088	0.706	0.988
WSe_2	0.036	0.116	0.701	0.863
$MoTe_2$	-0.262	-0.300	0.344	0.403
WTe_2	-0.112	-0.133	0.952	0.978

Table S1. Fundamental gap (E_g) and inverted gap (2δ) of monolayer transition metal dichalcogenides 1T'-MX_2 calculated by first-principles density-functional theory with PBE exchange-correlation functional and many-body perturbation theory within the G_0W_0 approximation.

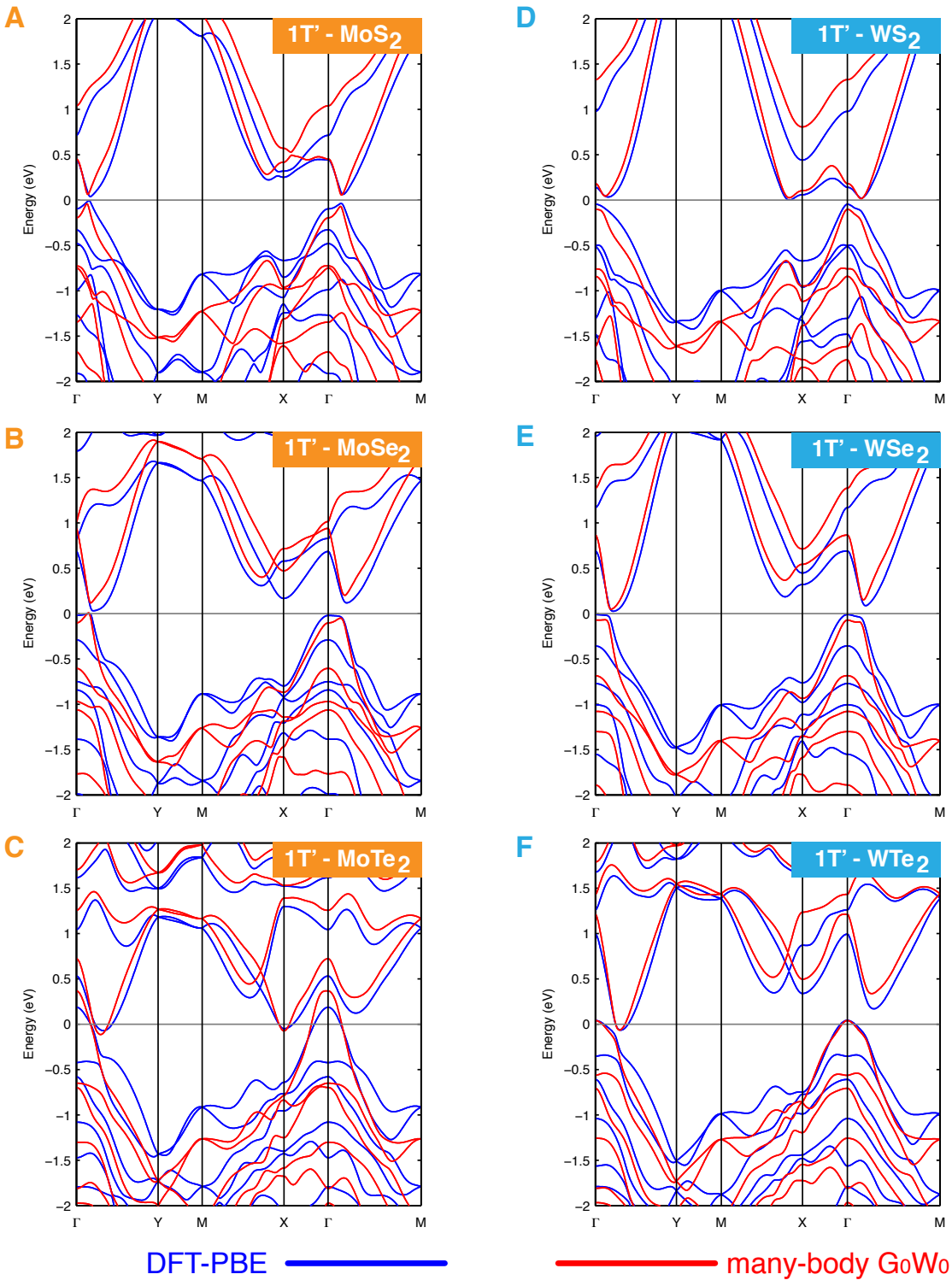

Fig. S1. Electronic band structure of monolayer transition metal dichalcogenides 1T'-MX_2. Blue lines stand for first-principles density-functional theory calculations. Red lines stand for many-body G_0W_0 theory calculations.

A — 1T' - MoS_2

Γ_i	parity ξ_{2m} of occupied bands	$\delta_i = \prod_m \xi_{2m}$
Γ	+ − − + − + + − − + + −	+
X	− + + − + − − + + − − +	−
Y	+ − + − + − + − + − + −	−
R	+ − + − + − + − + − + −	−
	Z_2 invariant ν: $(-1)^\nu = \prod_i \delta_i$	ν = 1

B — 1T' - $MoSe_2$

Γ_i	parity ξ_{2m} of occupied bands	$\delta_i = \prod_m \xi_{2m}$
Γ	+ − + − − + + − + − − +	+
X	− + + − + + − − + − − +	−
Y	+ − + − + − + + − + − −	−
R	− + + + − + − − + − + −	−
	Z_2 invariant ν: $(-1)^\nu = \prod_i \delta_i$	ν = 1

C — 1T' - $MoTe_2$

Γ_i	parity ξ_{2m} of occupied bands	$\delta_i = \prod_m \xi_{2m}$
Γ	+ − + − − + − + + − + − +	+
X	− + + − + − + − − + + − +	−
Y	+ − + − + − + − + − + − +	−
R	+ − + − + − + − + − + − +	−
	Z_2 invariant ν: $(-1)^\nu = \prod_i \delta_i$	ν = 1

D — 1T' - WS_2

Γ_i	parity ξ_{2m} of occupied bands	$\delta_i = \prod_m \xi_{2m}$
Γ	+ − − + − + + − − + + −	+
X	+ − + − − + − + + − − +	−
Y	− + + − + − + − − + + −	−
R	− + + + − + − + − + + −	−
	Z_2 invariant ν: $(-1)^\nu = \prod_i \delta_i$	ν = 1

E — 1T' - WSe_2

Γ_i	parity ξ_{2m} of occupied bands	$\delta_i = \prod_m \xi_{2m}$
Γ	+ − + − − + − + + − + −	+
X	− + + − + − + + − + − +	−
Y	− + + − − + + + − − + −	−
R	− + + + − − + + − − + −	−
	Z_2 invariant ν: $(-1)^\nu = \prod_i \delta_i$	ν = 1

F — 1T' - WTe_2

Γ_i	parity ξ_{2m} of occupied bands	$\delta_i = \prod_m \xi_{2m}$
Γ	+ − + − − + − + − + + −	+
X	− + + − + − + − + − − +	−
Y	− + + − − + + + − − + −	−
R	− + + + − − + + − − + −	−
	Z_2 invariant ν: $(-1)^\nu = \prod_i \delta_i$	ν = 1

Fig. S2. Parity tables for monolayer transition metal dichalcogenides 1T'-MX_2 at time-reversal invariant momenta, and the corresponding Z_2 invariants, ν. All Z_2 invariants are 1, indicating all six 1T'-MX_2 are topologically nontrivial. We choose the inversion center at the middle of the short M-M bond formed by two transition metal atoms.

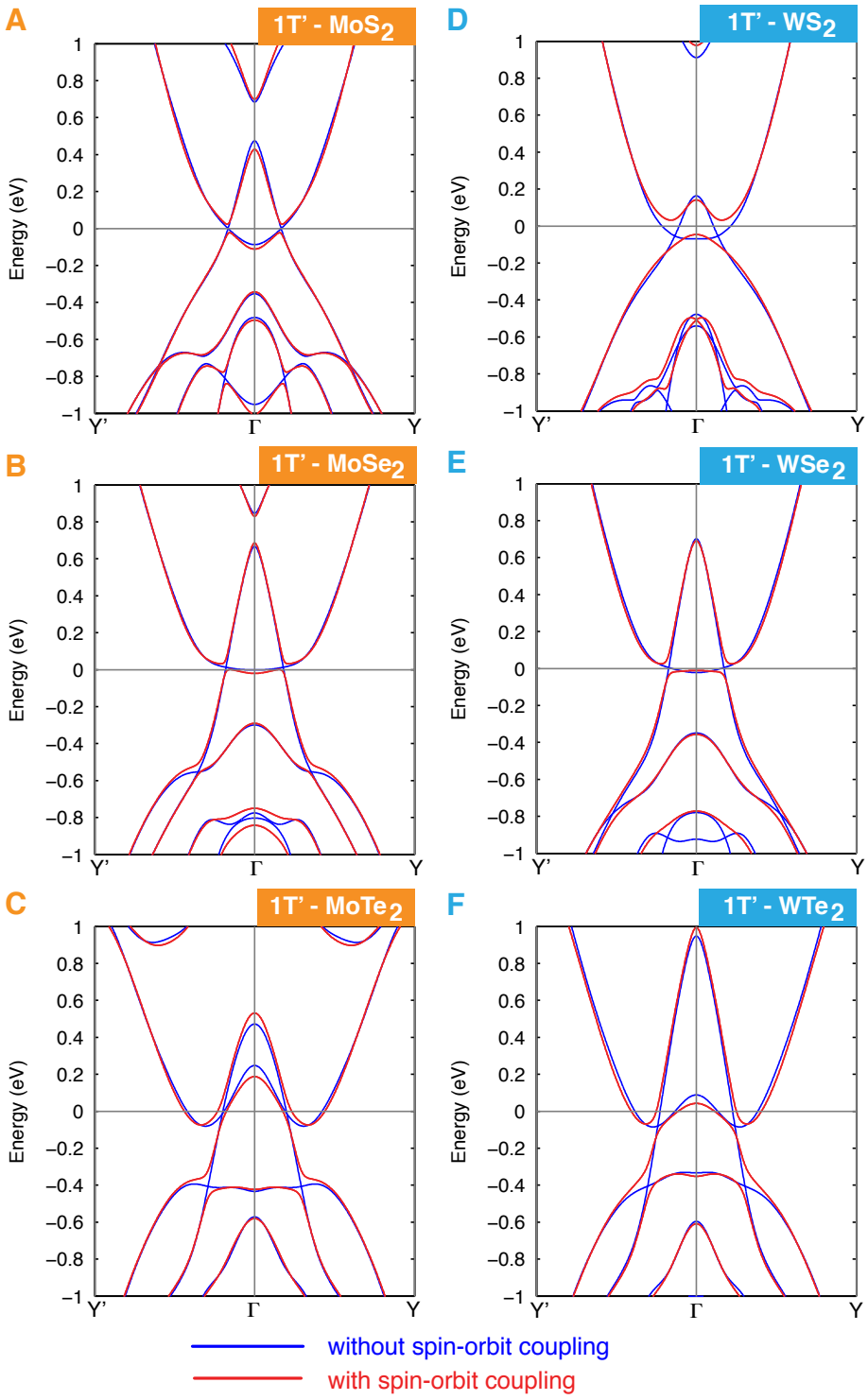

Fig. S3. Electronic band structure of monolayer transition metal dichalcogenides 1T'-MX_2 with and without spin-orbit coupling. The calculations were performed by first-principles density-functional theory with the PBE exchange-correlation functional.

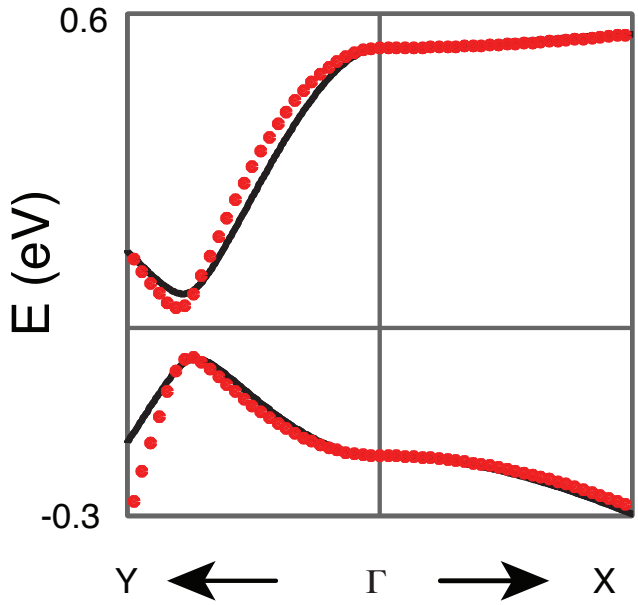

Fig. S4. Comparison of band structures obtained from first-principles GW calculation (black line) and the fitted $k \cdot p$ Hamiltonian (red dots) for 1T'-MoS_2.

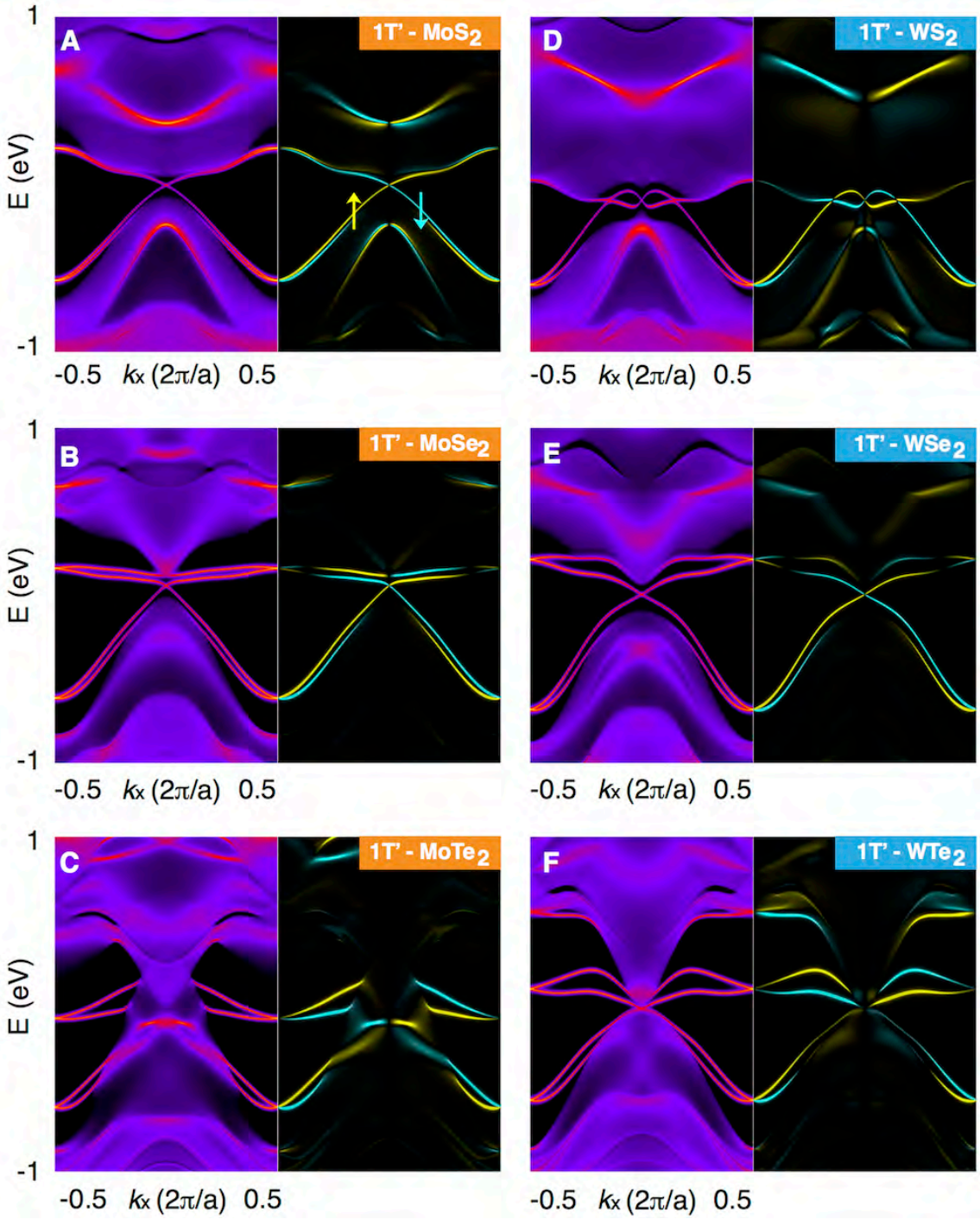

Fig. S5. Electronic structure of helical edge states in monolayer transition metal dichalcogenides 1T'-MX_2. For each MX_2, the left subpanel shows the density of states while the right subpanel shows the corresponding spin polarization. These helical edge states are a manifestation of nontrivial topology of monolayer 1T'-MX_2.

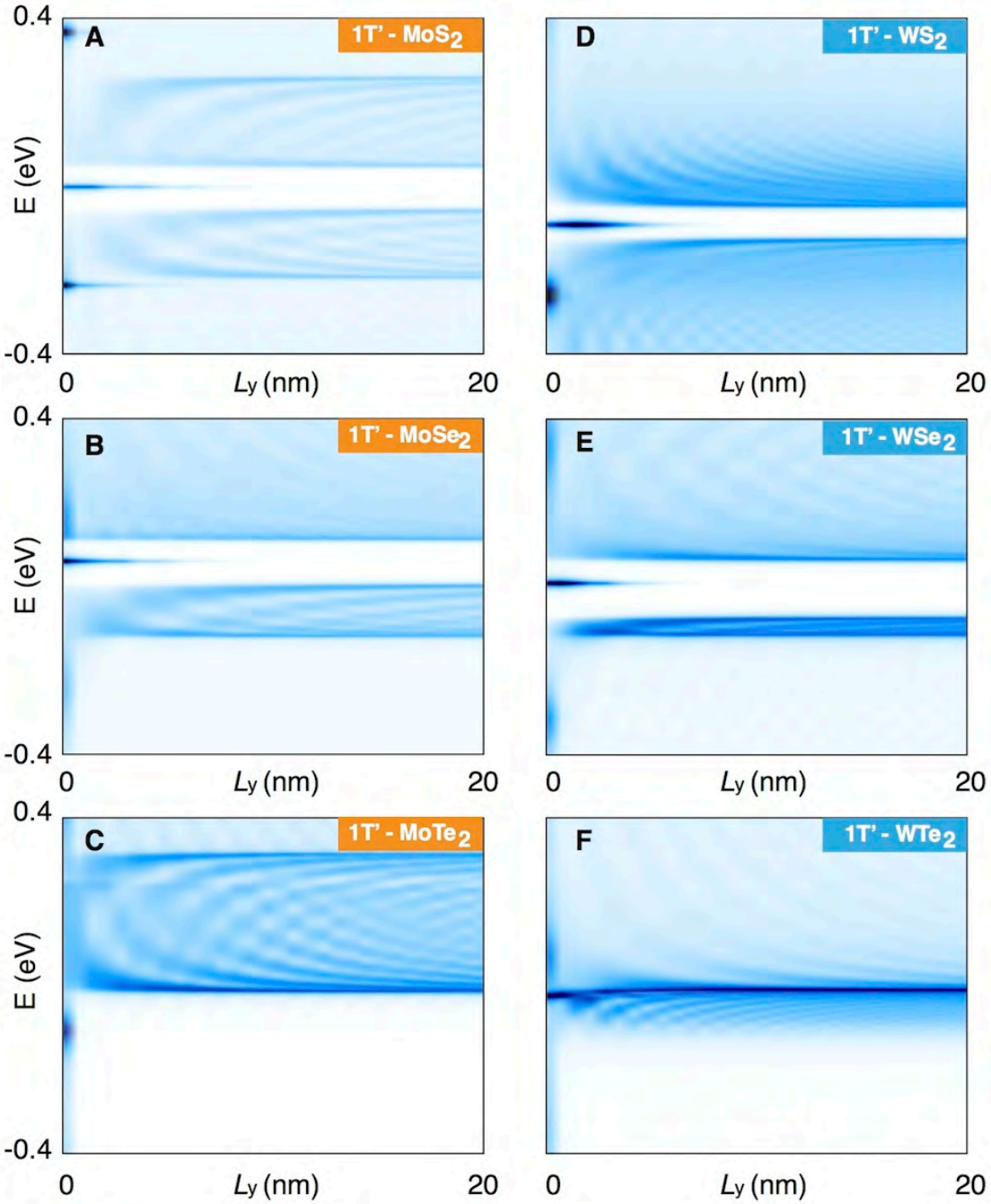

Fig. S6. Local density of states as function of penetration depth away from the edge at L_y=0 in monolayer transition metal dichalcogenide 1T'-MX_2. Due to the semi-metallic nature of 1T'-$MoTe_2$ and 1T'-WTe_2, local density of states from edge and bulk are entangled with each other. Therefore, the decay lengths of their edge states are not accessible.

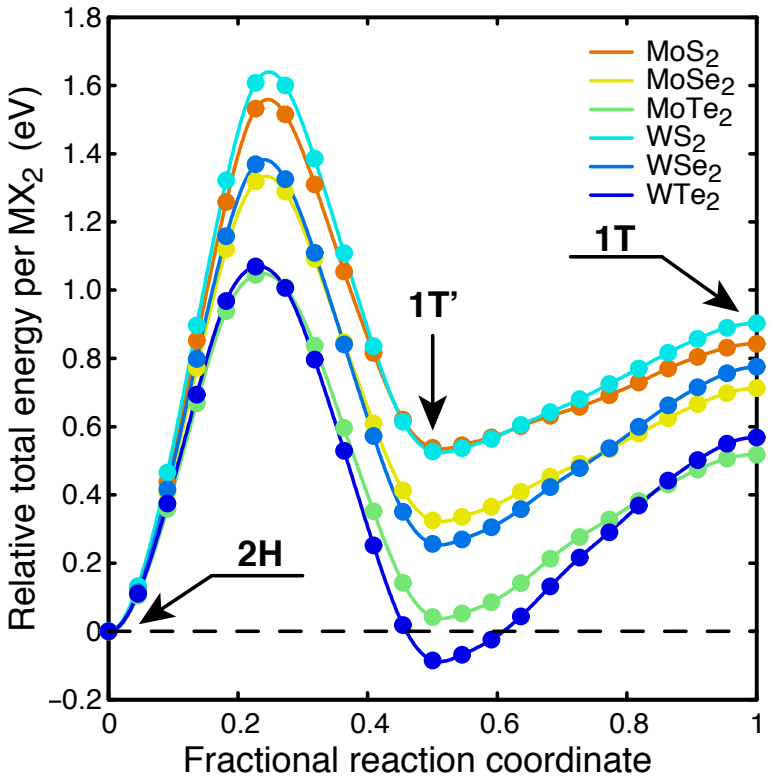

Fig. S7. Structural stability of monolayer transition metal dichalcogenide 1T'-MX_2. (**A**) Relative total energy per MX_2 as a function of fractional reaction coordinate.

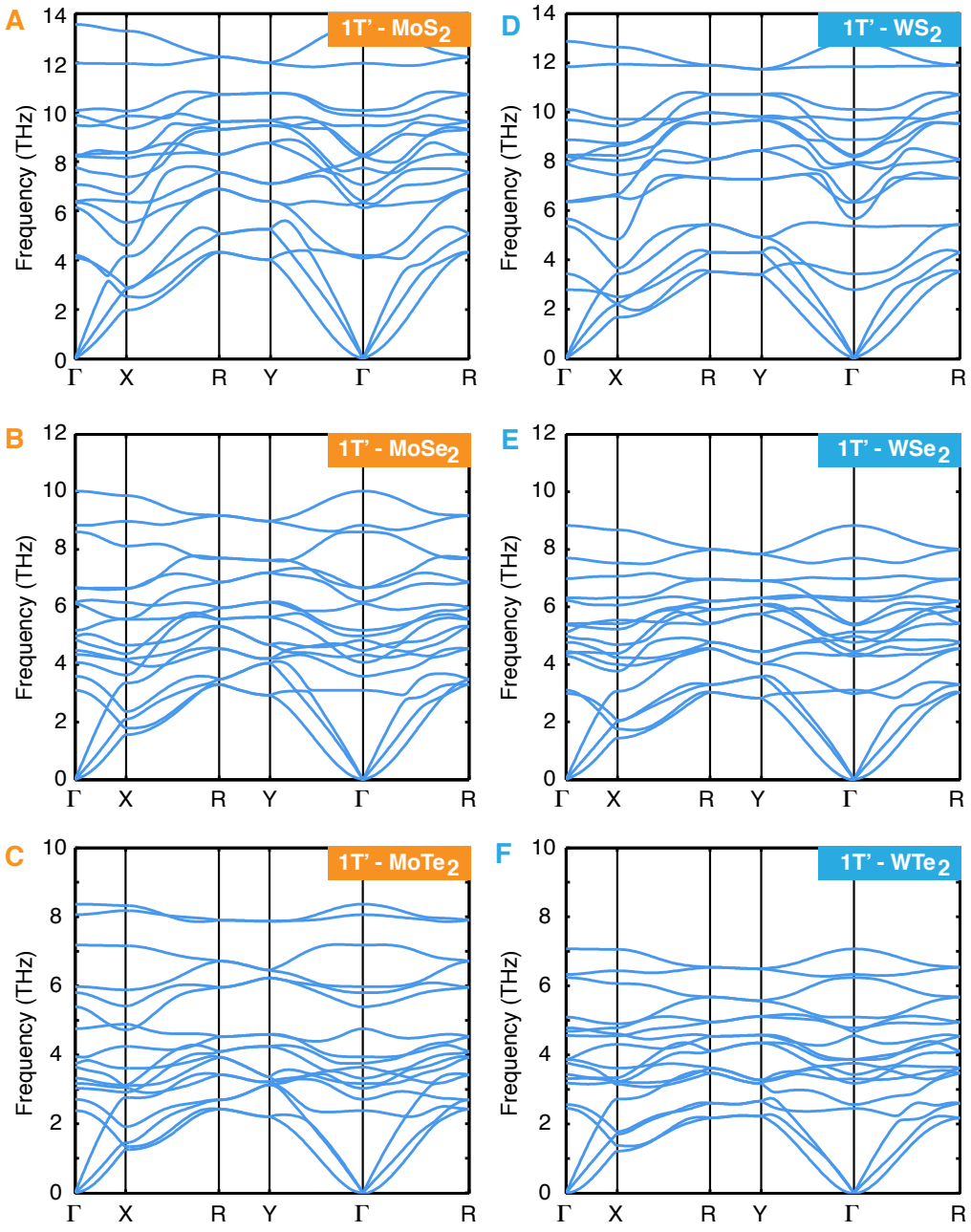

Fig. S8. Phonon dispersion curves of monolayer transition metal dichalcogenide 1T'-MX_2. The absence of imaginary frequency demonstrates the structural stability of all six monolayer 1T'-MX_2.

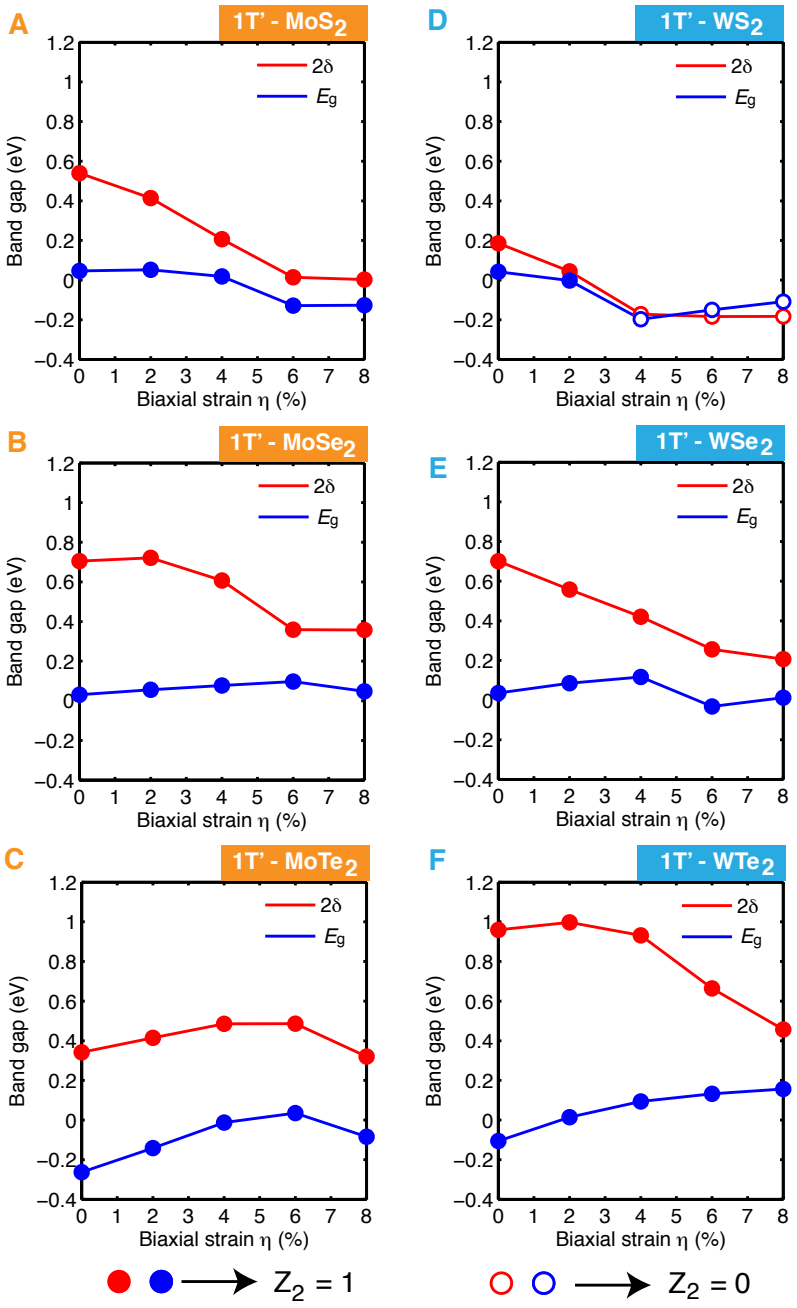

Fig. S9. Effect of biaxial strain on fundamental gap (E_g), inverted gap (2δ), and Z_2 invariant of 1T'-MX_2. Positive inverted gap (2δ) indicates Z_2=1 and positive E_g indicates insulator.

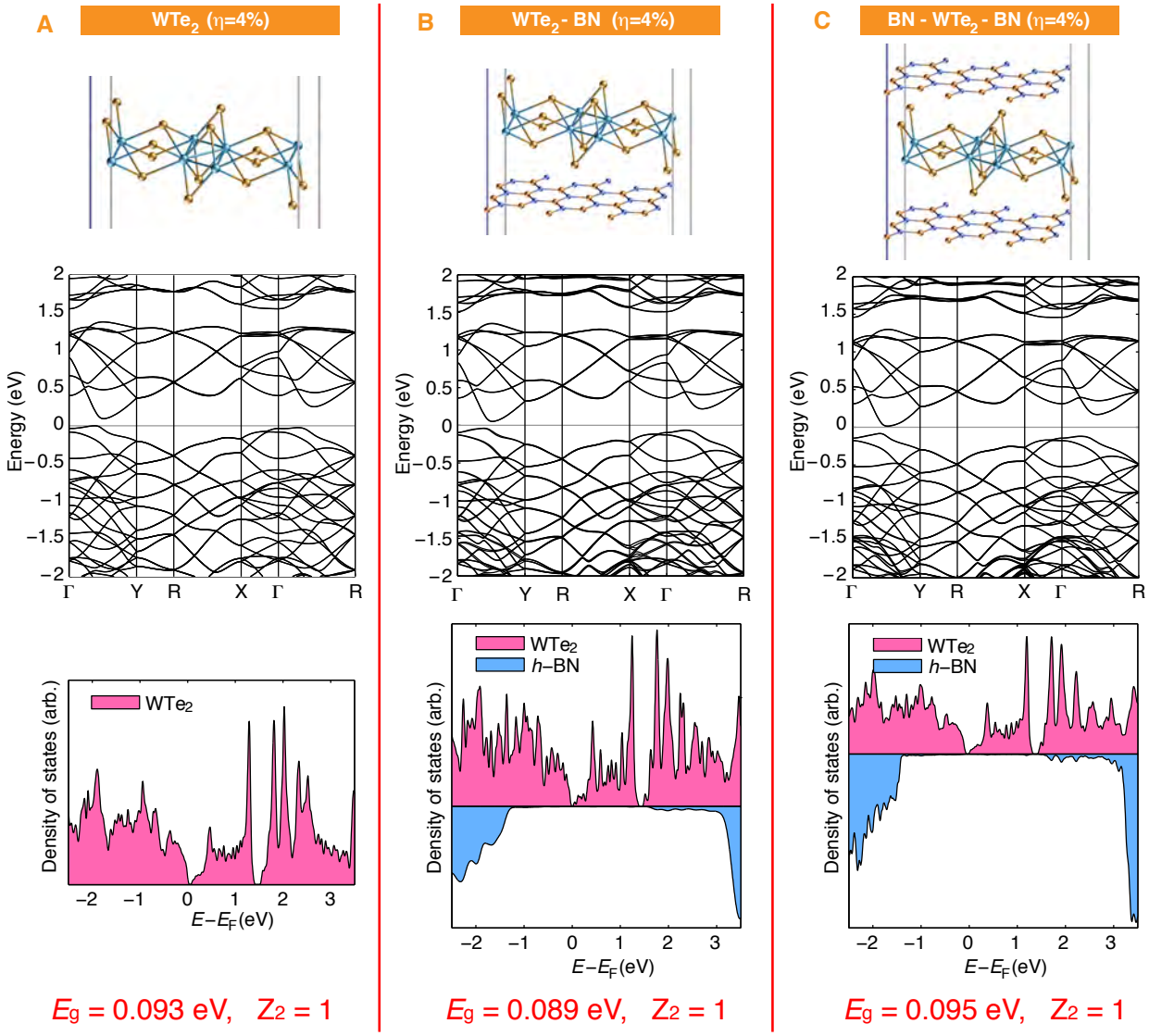

Fig. S10. Effect of van der Waals heterostacking with hexagonal BN monolayers on electronic structure, projected density of states, fundamental band gap (E_g), and Z_2 invariant of 1T'-WTe_2 under 4% biaxial strain. The supercell was constructed by 2x2 1T'-WTe_2 and $3\sqrt{3}\times3$ BN monolayers under 4% biaxial strain to minimize the lattice mismatch for first-principles calculations. **A**: biaxially-strained monolayer 1T'-WTe_2. **B**: strained 1T'-WTe_2 stacked on hexagonal BN monolayer. **C**: strained 1T'-WTe_2 sandwiched by two hexagonal BN layers. It clearly shows that BN monolayers have negligible effect on the electronic structure of 1T'-WTe_2 in a wide energy range around the Fermi level, demonstrating hexagonal BN sheets as ideal dielectric layers for the experimental realization of van der Waals heterostructure-based topological field effect transistor.

References:

1. P. Hohenberg, W. Kohn, Inhomogeneous Electron Gas. *Phys. Rev. B* **136**, B864-B864 (1964).
2. W. Kohn, L. Sham, Self-Consistent Equations Including Exchange and Correlation Effects. *Phys. Rev.* **140**, 1133-1133 (1965).
3. G. Kresse, J. Furthmuller, Efficiency of ab-initio total energy calculations for metals and semiconductors using a plane-wave basis set. *Comput. Mater. Sci.* **6**, 15-50 (1996).
4. G. Kresse, J. Furthmuller, Efficient iterative schemes for ab initio total-energy calculations using a plane-wave basis set. *Phys. Rev. B* **54**, 11169-11186 (1996).
5. P. E. Blöchl, Projector augmented-wave method. *Phys. Rev. B* **50**, 17953-17979 (1994).
6. J. P. Perdew, K. Burke, M. Ernzerhof, Generalized gradient approximation made simple. *Phys. Rev. Lett.* **77**, 3865-3868 (1996).
7. D. C. Langreth, M. J. Mehl, Beyond the local-density approximation in calculations of ground-state electronic-properties. *Phys. Rev. B* **28**, 1809-1834 (1983).
8. A. D. Becke, Density-functional exchange-energy approximation with correct asymptotic-behavior. *Phys. Rev. A* **38**, 3098-3100 (1988).
9. H. Monkhorst, J. Pack, Special Points for Brillouin-Zone Integrations. *Phys. Rev. B* **13**, 5188-5192 (1976).
10. L. Hedin, New Method for Calculating the One-Particle Green's Function with Application to the Electron-Gas Problem. *Phys. Rev.* **139**, A796-A823 (1965).
11. M. S. Hybertsen, S. G. Louie, Electron correlation in semiconductors and insulators: Band gaps and quasiparticle energies. *Phys. Rev. B* **34**, 5390-5413 (1986).
12. M. P. L. Sancho, J. M. L. Sancho, J. Rubio, Highly convergent schemes for calculation of bulk and surface Green-functions. *J. Phys. F* **15**, 851-858 (1985).
13. N. Marzari, D. Vanderbilt, Maximally localized generalized Wannier functions for composite energy bands. *Phys. Rev. B* **56**, 12847-12865 (1997).
14. X. Qian, J. Li, L. Qi, C.-Z. Wang, T.-L. Chan, Y.-X. Yao, K.-M. Ho, S. Yip, Quasiatomic orbitals for ab initio tight-binding analysis. *Phys. Rev. B* **78**, 245112-245112 (2008).
15. L. Fu, C. L. Kane, Topological insulators with inversion symmetry. *Phys. Rev. B* **76**, 045302-045302 (2007).
16. T. Fukui, Y. Hatsugai, Quantum Spin Hall Effect in Three Dimensional Materials: Lattice Computation of Z_2 Topological Invariants and Its Application to Bi and Sb. *J. Phys. Soc. Jpn.* **76**, 053702-053702 (2007).